LAWRENCE
LIVERMORE
NATIONAL
LABORATORY

LLNL-PROC-486491

Two-dimensional Imaging Velocity Interferometry: Technique and Data Analysis

D. J. Erskine, R. F. Smith, C. Bolme, P. Celliers, G. Collins

June 10, 2011

APS Shock Compression Condensed Matter
Chicago, IL, United States
June 26, 2011 through July 1, 2011

Disclaimer

LLNL-PROC-486491
APS/SCCM meeting, Chicago 2011

TWO-DIMENSIONAL IMAGING VELOCITY INTERFEROMETRY: TECHNIQUE AND DATA ANALYSIS

David J. Erskine, R. F. Smith, C. Bolme, P. Celliers, G. Collins

erskine1@llnl.gov, L-487, Lawrence Livermore Nat Lab, Livermore, CA 94550

Abstract. We describe the data analysis procedures for an emerging interferometric technique for measuring motion across a two-dimensional image at a moment in time, i.e. a snapshot 2d-VISAR.
Keywords: VISAR, velocity interferometry
PACS: 07.60.Ly

INTRODUCTION

Velocity interferometers (VISAR) measuring target motion to high precision have been an important diagnostic in shockwave physics for many years[1, 2, 3, 4]. Until recently, this diagnostic has been limited to measuring motion at points or lines across a target. We introduce an emerging interferometric technique for measuring motion across a two-dimensional image, which could be called a snapshot 2d-VISAR.

If a sufficiently fast movie camera technology existed, it could be placed behind a traditional VISAR optical system and record a 2d image vs time. But since that technology is not yet available, we use a CCD detector to record a single 2d image, with the pulsed nature of the illumination providing the time resolution.

Consequently, since we are using pulsed illumination having a coherence length shorter than the VISAR interferometer delay ($\sim$0.1 ns), we must use the white light velocimetry configuration to produce fringes with significant visibility[5, 6, 7]. In this scheme, two interferometers (illuminating, detecting) having nearly identical delays are used in series, with one before the target and one after. This produces fringes with at most 50% visibility, but otherwise has the same fringe shift per target motion of a traditional VISAR.

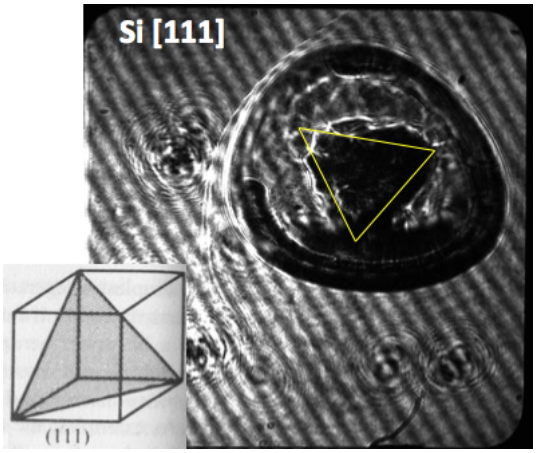

FIGURE 1. Trigonal symmetry of a spherical wave emerging from 1 mm thick Si along the [111] direction is immediately apparent with an 2d-imaging VISAR. The 2d-VISAR allows a whole new world of data not accessible by point or line-VISARs. Field of view $\sim$1 mm.

The 2d-VISAR observes a new world of information (Fig. 1) about shock behavior not readily accessible by traditional point or 1d-VISARS, simultaneously providing both a velocity map and an "ordinary" snapshot photograph of the target. The 2d-VISAR has been used to observe nonuniformities in NIF related targets (polycrystalline diamond, Be)[8, 9], and in Si (Fig. 1) and Al (Fig. 4).

DATA PROCESSING STEPS

1. Split into quads. The original 4096x4096 sized image from the CCD detector is split into four quadrants of 2000x2000 size, rotating to overlay.

2. Overlay quads. Sections of each quadrant are correlated to find rotation, translation, magnification. The result is a stack of images having four intensities S_n per pixel. The correlation peak width can be $\sim$3 pixels, indicating focus quality. Correlations usually can be done on shot exposure.

3. Lissajous analysis. A 1d-lineout is taken, usually in the undriven area where the fringe phase is well behaved, perpendicular to the bias fringes, and $>$1 period ($\sim$100 pixels). A Lissajous plot of F (Fig. 6, top) is made of the combined four channels (via Eqs. 2-10) and the gains and offsets adjusted until the Lissajous is centered and circular. Under changing I it helps to plot $|F|$ vs I plot (Fig. 6, bottom) for best linearity.

3b. (Optional) Spatial dependence. Repeat above step at different locations to find any spatial dependence to optimal gains. Often the spatial dependence is weak and we approximate gains as constants for expediency. Appearance of the bias fringe periodicity or 2nd harmonic in any 2d-outputs (below) indicates gains not optimal.

4. Math applied to 2d data. The optimal gains are applied to the 2d data via Eqs. 2-12 to produce intensity $I(x,y)$, the complex fringing field $F(x,y)$, wrapped phase $\theta(x,y)$, and magnitude $|F(x,y)|$.

4b. (Optional) Removal of bias phase slope. The constant slope in phase due to due tilted interferometer mirror causes the FFT of F to translate. Thus one can easily remove the bias slope by identifying what would be the DC spike, translating the FFT so that this spike is at the origin. However, the bias slope is useful to keep for Lissajous display purposes, and for manifesting contours in the wrapped phase map (Fig. 4), so we often postpone removing it.

5. (Optional) Fourier power spectra The Fourier spectrum of $F(x,y)/|F(x,y)|$ can be immediately taken (not needing the problematic unwrapping step below), to characterize the phase (velocity) roughness. An FFT of $I(x,y)$ characterizes the ordinary image. The FFT can be taken on subsets of the image to provide some spatial dependence.

6. Unwrapping of phase map. Where integer fringe skips are encountered they are restored to produce a continuous surface of phase. However, noise in low intensity areas (due to laser speckle) produces areas of wildly fluctuating phase which confuses most algorithms. (Hence the granular appearance of Fig. 7.) This problem is still being explored.

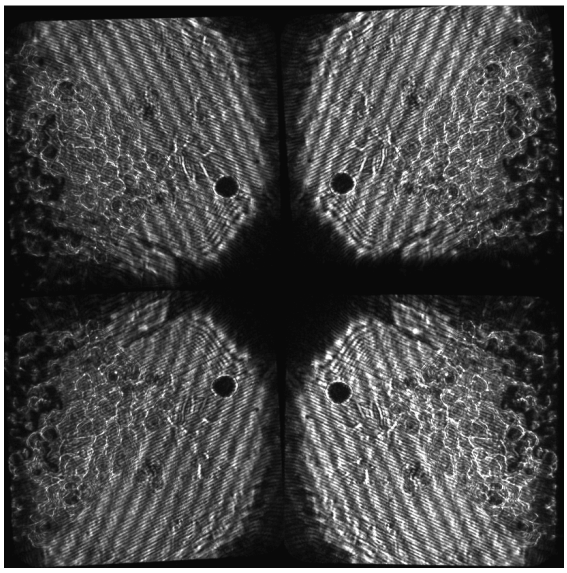

FIGURE 2. Raw image from CCD detector records four interferometer outputs ideally having 90° phase interval between them.

Supporting equations

The interferometer output for the channels n is

$$S_n(x,y) = I(x,y)\{1+0.5\gamma\cos 2\pi[\theta(x,y)+\phi_n]\} \quad (1)$$

The four output channel phases ϕ_n are ideally in 90° intervals, but often irregular by $\sim$30°. Irregularity is handled by the obliquity correction Eq. 9. The visibility γ decreases from 1 by interferometer misalignment, or target surface quality under shock loading. The 0.5 maximum fringe contrast is appropriate for the partial coherence of white light velocimetry. The target reflected intensity is $I(x,y)$, and detected intensity post-interferometer $S(x,y)$. Channel dependent transmission loss through the optics is represented by gain coefficients in Eqs. 2-4 etc.

The equations below for combining the four detected signals S_n into fringing F and nonfringing I outputs are the same for each pixel, and thus we can omit the (x,y). As a first approximation the gains g_n

and offsets h_0, v_0 are constants, but should eventually model any slight spatial variation of beam intensities.

$$S'_0 = (g_{02}\, S_0 + h_0) g_{hv} \quad (2)$$
$$S'_1 = (g_{13}\, S_1 + v_0) \quad (3)$$
$$S'_2 = g_{hv} S_2 \quad (4)$$
$$S'_3 = S_3 \quad (5)$$

The two intermediate outputs are the nonfringing intensity I and the complex fringing field F

$$I = 0.25(S'_0 + S'_1 + S'_2 + S'_3) \quad (6)$$

$$F = (S'_0 - S'_2) + i(S'_1 - S'_3) \quad (7)$$

It is useful to confirm that $I_v = S'_0 + S'_2$ appears like $I_h = S'_1 + S'_3$. Otherwise you have a bad channel.

The obliquity transform fixes irregular phase steps. Temporarily change coordinates to a 45° axis, and apply an astigmatic correction g_q along the new axis. Typically $g_q \sim 0.6$ to 1.

$$\Re F \leftarrow 0.5\{(g_q+1)\Re F + (g_q-1)\Im F\} \quad (8)$$
$$\Re I \leftarrow 0.5\{(g_q-1)\Re F + (g_q+1)\Im F\} \quad (9)$$
$$F \leftarrow \Re F + i\Im F \quad (10)$$

The offsets h_0, v_0, translate the Lissajous ($\Im F$ vs $\Re F$). The horizontal to vertical astigmatism g_{hv} stretches the Lissajous. The left/right asymmetry g_{02} and up/down asymmetry g_{13} are degenerate with offsets h_0, v_0 when Lissajous magnitude ($|F|$) is constant, and are only relevant when the magnitude changes significantly. In that case, one first adjusts the offsets to center the weakest intensity portions of the Lissajous, and then uses g_{02} and g_{13} to center the outer portions.

The gains and offsets are adjusted until the Lissajous is centered and circular. To make this determination independent of fluctuating I, one plots $|F|$ vs I and minimizes deviations from linearity.

After one is satisfied with choice of gains and offset (by obtaining a circular and centered Lissajous), then the magnitude $|F|$ and phase θ is

$$|F|^2 = (\Im F)^2 + (\Re F)^2 \quad (11)$$

$$2\pi \tan\theta = \frac{\Im F}{\Re F} \quad (12)$$

obtained for every pixel. This will be proportional to the target velocity as in a traditional VISAR (in the short etalon approximation).

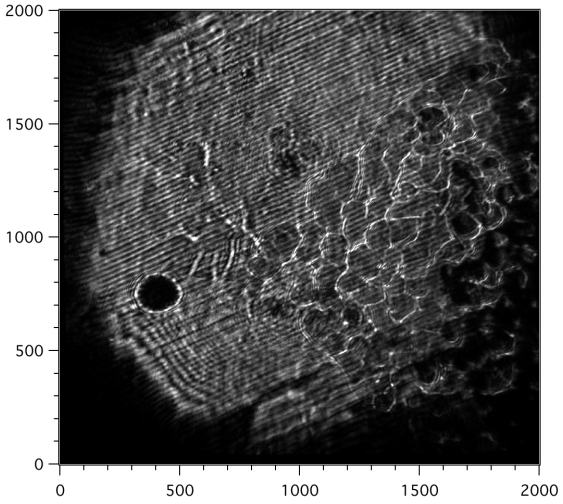

FIGURE 3. The snapshot "ordinary" image of target, $I(x,y)$, simultaneous with phase measurement (Fig. 4), formed by summing the four quadrature images so that fringes cancels. Field of view is ~1 mm per 2000 pixels. Target is 50 μm of aluminum facing vacuum. The fine striations are machining scratches. The corner of the square target is centered on the image.

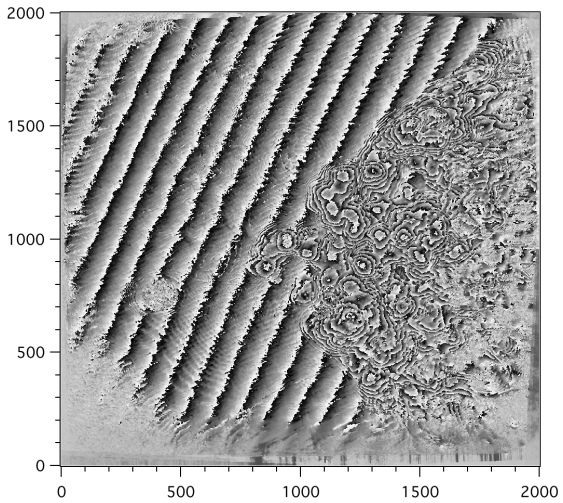

FIGURE 4. Snapshot phase (velocity) map of target simultaneous to ordinary image (Fig. 3). The interesting velocity variations in the target may be due to aluminum granular domains. The undriven side of the image has the uniform bias fringes. Phase is wrapped.

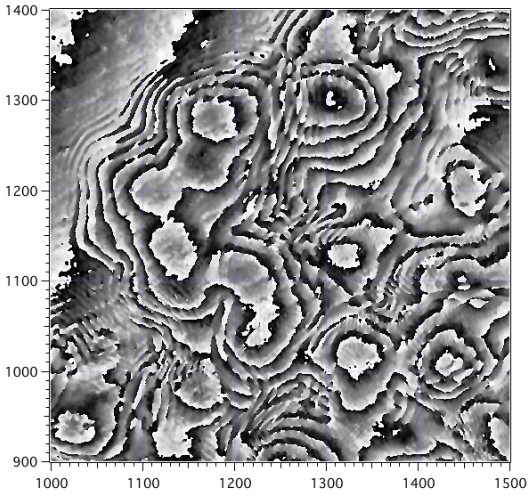

FIGURE 5. Wrapped phase map subset.

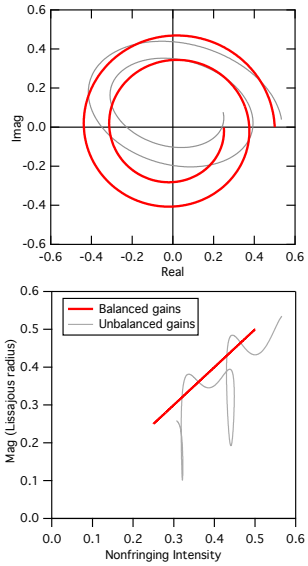

FIGURE 6. Optimal gain parameters (red curves) produce the most circular Lissajous, $\Im F$ vs $\Re F$ (top), and most linear $|F|$ vs intensity I (bottom).

ACKNOWLEDGMENTS

This work performed under the auspices of the U.S. Department of Energy by Lawrence Livermore National Laboratory under Contract DE-AC52-07NA27344.

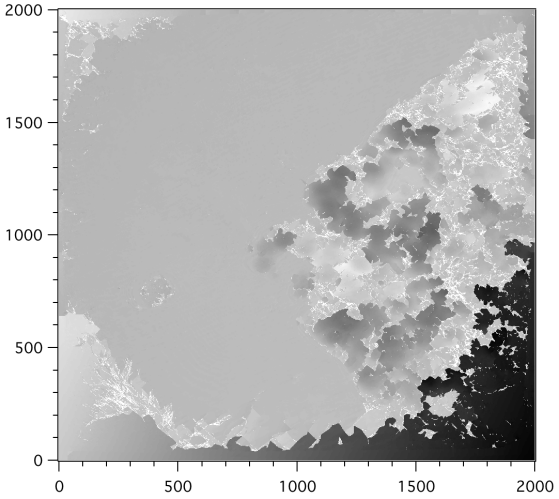

FIGURE 7. Phase map after some fringe skips removed by a commercial algorithm (Wavemetrics, Igor application). Algorithm is confused by many regions of low intensity where noise causes wild variation in phase.

REFERENCES

1. Barker, L., and Hollenbach, R., *J. Appl. Phys.*, **43**, 4669–4675 (1972).
2. Hemsing, W., *Rev. Sci. Instr.*, **50**, 73–78 (1979).
3. Hemsing, W., Mathews, A., Warnes, R., George, M., and Whittemore, G., "VISAR: Line-Imaging interferometer," in *Shock Compression of Condensed Matter-1991*, edited by S. Schmidt, North-Holland, 1992, pp. 767–770.
4. Dolan, D., *Sandia Report*, **SAND2006-1950** (2006).
5. Erskine, D., and Holmes, N., *Nature*, **377**, 317–320 (1995).
6. Erskine, D. J., and Holmes, N. C., "Imaging White Light VISAR," in *High Speed Photography and Photonics*, edited by D. L. Paisley, 1997, vol. 2869 of *SPIE*, pp. 1080–1083.
7. Celliers, P. M., Erskine, D. J., Sorce, C. M., Braun, D. G., Landen, O. L., and Collins, G. W., *Review of Scientific Instruments*, **81**, 035101–+ (2010).
8. Celliers, P. M., Erskine, D. J., Prisbrey, S. T., Braun, D. G., Richards, J. B., Sorce, C. M., Collins, G. W., Wallace, R. J., Landen, O. L., and Nikroo, A., *APS Mtg. Abstr.*, pp. 6009–+ (2007).
9. Celliers, P. M., Erskine, D. J., Braun, D. G., Prisbrey, S. T., Collins, G. W., Wallace, R. J., Landen, O. L., Biener, J., Hamza, A. V., Wild, C., Woerner, E., and Nikroo, A., *APS Mtg. Abstr.*, pp. 4005–+ (2009).